JOURNAL OF AIRCRAFT
Vol. 41, No. 3, May–June 2004

Numerical Analysis of Aerodynamic Control of Delta Wing by Microflap

Takeshi Kaiden* and Yoshiaki Nakamura†
Nagoya University, Nagoya 464-8603, Japan

In this study, computational fluid dynamics (CFD) simulation is performed to clarify the mechanism of rolling moment generation due to a delta wing with a microflap. As a result, it was found that a leading-edge separation vortex is displaced by changing the location of the microflap at the leading edge. The positive rolling moment was produced for installation of the flap in the lower part of the leading edge, whereas the negative rolling moment was produced in the upper part. These characteristics are similar to experimental data. Detailed observation of simulated results in turbulent case shows that the leading-edge separation vortex slightly moves toward the outboard direction in the former case, whereas it does not move toward inboard, but becomes diffusive, in the latter case. The mechanism of the rolling moment generation seems to have a slight discrepancy between CFD results and the explanation based on the experimental data. The rolling moment actually depends not only on the vortex location, but also on its magnitude and size. Finally, there were no large differences in rolling moment between calculated results with and without a turbulence model.

Nomenclature

L = total length of delta wing
X = distance from apex toward downstream in the body-axis system
θ = angle from the bottom point to the foot of flap in leading-edge cross section

Introduction

RECENTLY microelectromechanical systems (MEMS) have been studied and developed worldwide. In aerospace fields, turbulent flows and separated flows, which are basically very difficult to control, have been tackled by using MEMS. The objective of the former applications is to reduce friction drag, whereas that of the latter is to arbitrarily change the attitude of aircraft, where a micromachine with the same dimension as the boundary layer is placed at the location where aerodynamic forces have a high sensitivity.[1–4] In one of these applications, a microflap was installed at the leading edge of a delta wing so that the rolling moment was generated by changing the position of a leading-edge separation vortex.[1] This suggests that such a microflap has a potential to replace conventional flaps in the near future, which has a great advantage over the conventional flaps in the following respects: 1) lighter airplane weight, 2) lower aerodynamic loads acting on a flap system, 3) simpler structural design, and 4) smaller radar cross section of an airplane.

The present research is a numerical analysis of aerodynamic control for a delta wing with a microflap as a MEMS application. The microflap is installed at the leading edge of the delta wing to change the characteristics of a leading-edge vortex generated above the upper surface. More specifically, by CFD, the effects of the flap installation location on the leading-edge vortex are examined for cases both with and without a turbulent model. Although this problem has been studied by several researchers,[5–6] a more detailed analysis remains to be made for clarifying the mechanism. This is the objective of the present study.

The basic concept mentioned in Ref. 1 is briefly reviewed in the first section. Computational methods such as grid generation and the flow solver employed in this study are described in the second section. Before showing computational results of the microflap, the validation of the computation is presented from the viewpoint of applicability to incompressible flow analysis of the present compressible scheme. In the subsequent sections, computational results of the microflap will be shown and discussed, and finally concluding remarks are made.

Basic Concept

A leading-edge separation vortex is generated by increasing the angle of attack of a delta wing, which contributes to production of lift force on the wing. When a microflap, the shape of which is a rectangle, is placed at the leading edge, the leading-edge vortex is forced to move in the lateral direction so that the rolling moment will be produced on the wing, provided that the other wing half has no such flap. Figure 1 shows this concept schematically.

When the flap is set at a lower part of the leading edge, that is, at a small value of θ, the region with suction force due to the leading-edge separation vortex (LESV) moves toward the wing tip so that rolling moment is generated to lift this wing half. On the other hand, when the flap is set at an upper part of the leading edge, that is, at a larger value of θ, the suction region due to the LESV moves toward the wing root so that the wing tip will be brought down. These characteristics have been verified by other researchers' wind-tunnel testing.[1]

Computational Method

Computational Geometry

The computational geometry used in this study is shown in Fig. 2. The delta wing has a swept angle of 56.5 deg, which is the same as that of Ref. 1, and the full chord length and thickness of the wing are 30 and 1.47 cm, respectively. This wing is relatively thicker than a usual delta wing. A microflap with a chord length of 2 mm is placed at the leading edge from $X/L = 0.1$ to $X/L = 0.98$, which is close to the experiment.

Grid Generation

An overset grid system with a mother grid for the delta wing and a child grid for the flap is applied to this problem, because it can easily treat the wing–flap combination system. Each quantity is

Received 9 September 2002; revision received 20 June 2003; accepted for publication 5 September 2003.

*Graduate Student, Fluid Dynamics Laboratory, Department of Aerospace Engineering. Member AIAA.
†Professor, Fluid Dynamics Laboratory, Department of Aerospace Engineering. Member AIAA.

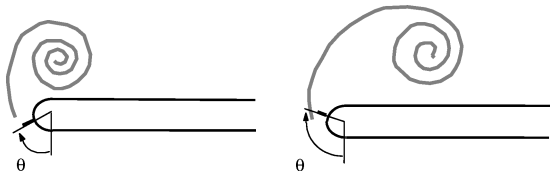

a) Lower flap location b) Upper flap location

Fig. 1 Basic concept.

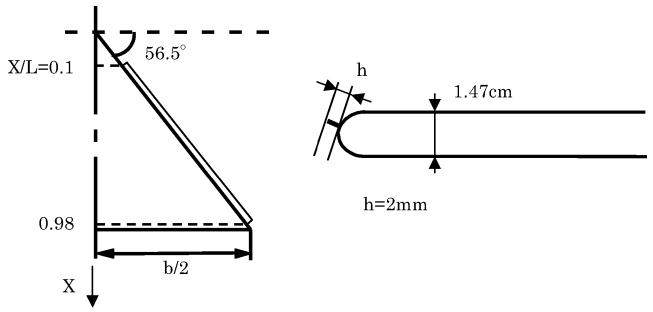

Fig. 2 Computational geometry ($L = 30$ cm, $b = 40.35$ cm).

communicated between these two grids in the process of flow calculation. This overset grid system has been validated so far in various applications.[7–9] The comparison between the present CFD code and the experiments of Boeing regarding forces, pressure distributions, and oil flow has been carried out in Ref. 9. The results show good agreement between the CFD and experiments.

The grids are generated via an algebraic interpolation method only for a half model, which is shown in Fig. 3. The topology of the grid is C-O type, and the number of grid points for the wing is 210 points in the streamwise direction, 191 points in the circumferential direction, and 65 points in the normal direction, which total 2.6×10^6 grid points. On the other hand, the microflap has 115 points in the streamwise direction, 163 points in the circumferential direction, and 40 points in the normal direction, which total 7.5×10^5 grid points. Thus, the total number of grid points is 3.35×10^6.

Flow Solver

The governing equations employed in this study are the three-dimensional thin-layer Reynolds-averaged Navier–Stokes equations. Roe's flux difference splitting with MUSCL is applied to convective terms.[10] The LU-ADI implicit method is adopted in time integration, and the local time stepping is employed to accelerate the convergence to steady-state solutions. Although the local time stepping is adopted, the unsteady phenomenon does not become problematic because the time step is very small. These schemes have been already evaluated by Fujii and Obayashi for an unsteady vortical flow.[10]

For a turbulence model, the Baldwin–Lomax algebraic model[11] with Degani–Shiff (DS) correction[12] was used to capture the phenomenon of large flow separation. This turbulence model is effective from the viewpoint of computational accuracy and efficiency.

A computational procedure with the Chimera technique is described in Fig. 4. First, the value of each quantity in a hole region of the mother grid is interpolated from that on the child grid (process A). After this interpolation, flow computation is performed on the mother gird except for the hole (process B). Then, quantities in the hole on the child grid are interpolated from the mother gird (process C). Finally, the flow is computed on the child grid (process D). This process is repeated until a converged solution is obtained.

Computational Conditions

Regarding flow conditions, the freestream Mach number is $M = 0.3$, which is different from that of the wind-tunnel test in Ref. 1, where Mach number is around 0.1. Use of the parameter $M = 0.3$ was decided by considering a computational efficiency in applying a compressible solver to an incompressible flow problem.

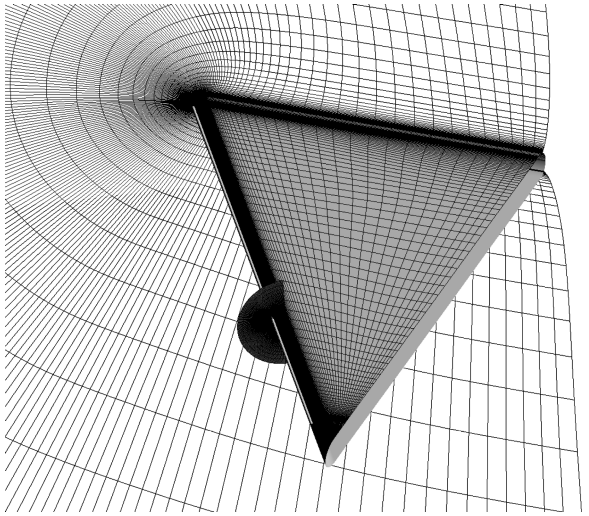

a) Overview

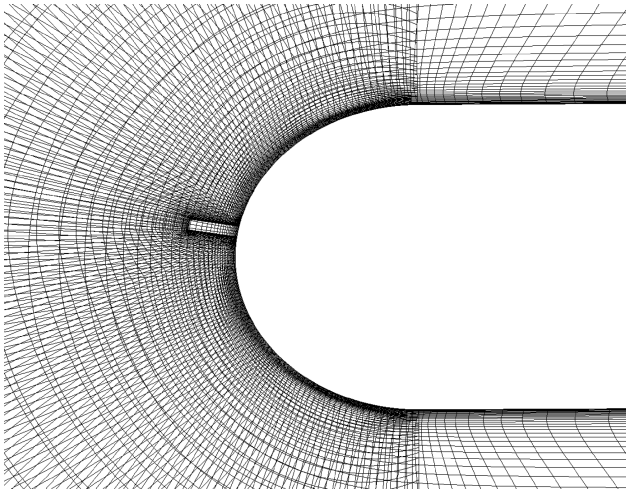

b) Cross section

Fig. 3 Computational grid.

The Reynolds number based on the total chord length is 5.3×10^5, which corresponds to the test condition of Ref. 1. Detailed flow characteristics of Ref. 1 are not known (for example, the flow is turbulent or laminar); both turbulent and laminar computations are performed in the present study. Actually the crossflow separation point around the leading edge seems to depend on whether the flow is turbulent or laminar.

The attack angle of the wing model is $\alpha = 20$ deg, and the location of the microflap is measured as the angle from the lowest point of the leading edge. In the present study, the flap is installed between $\theta = 20$ and 160 deg.

Because the flow at $\alpha = 20$ deg becomes intrinsically unsteady, all data from CFD simulation are averaged in time in every postprocessing.

Validation for Incompressible Computation

To validate the present compressible scheme for the analysis of incompressible flow, two-dimensional computation has been carried out. The computational geometry is a multi-element airfoil referred to as Boeing model C. This geometry has been frequently used for the validation of CFD analysis. The computation is performed via the compressible scheme with the Chimera approach, which is similar to the present three-dimensional computation. The grid system is shown in Fig. 5. The total number of the grids is about 8.2×10^5. The computational results are shown in Fig. 6 along with the experimental data. The computational conditions are a freestream Mach number of 0.2 and a Reynolds number of 2.83×10^6 based on the

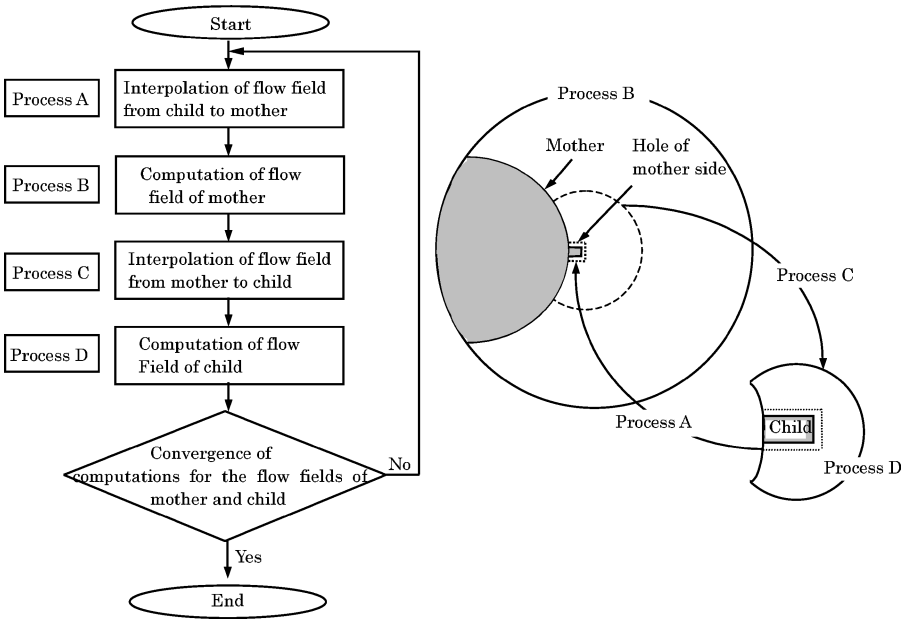

Fig. 4 Computational procedure.

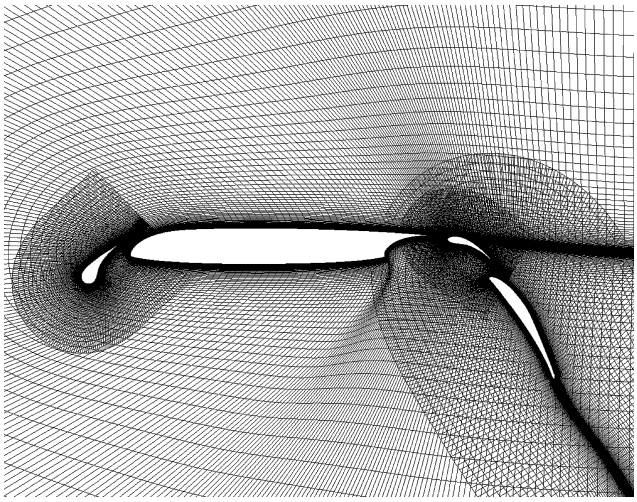

Fig. 5 Computational grid for multi-element airfoil.

chord of the retracted airfoil. Figures 6a and 6b are surface-pressure distribution at angles of attack of 0 and 12.2 deg, respectively. The comparison between the computation and experiment shows good agreement, which indicates that the present compressible scheme can be applied to incompressible flow analysis.

Computational Results for Microflap

Case 1: Turbulent Flow

Change in Rolling Moment Due to Flap

Figure 7 shows a comparison between results from the present CFD analysis and experimental data of Ref. 1 with regard to change in rolling moment produced on the delta wing and, more specifically, the difference in rolling moment between flap-on and flap-off cases, due to each flap location in the turbulent flow case.

Results with the DS model are qualitatively similar to the experimental data, as shown in Fig. 7. That is, ΔCR (the difference in rolling moment between cases with and without microflap) takes a positive value at a lower installation angle, that is, a rather small value of θ, whereas it takes a negative value at an upper angle.

However, the peak value and its location are slightly different from each other. The reason for the discrepancy of the location is due to the difference in microflap angle between the CFD analysis and the experiment. The installation angle of the microflap in the CFD model is normal to the surface, whereas that of the experiment does not seem to be normal. The microflap in the experiment is made of a thin steel metal so that its length can be freely adjusted (see Fig. 8). Therefore, the installation angle is not normal to the surface. In addition, it will be bent in the leeside direction due to a relatively large dynamic pressure. For these reasons, the installation location in the experiment will correspond to a larger angle in the computation. Therefore, the installation locations with the maximum and minimum ΔCR in the experiment should be smaller than those of the CFD results.

In addition, the peak value in the experiment will become different from that in the CFD for the same reason. The flow separation depends on microflap angle. The microflap in the CFD analysis, which is installed normal to the surface, disturbs the LESV more than that in the experiment. Consequently, in the CFD results the vortex lift becomes smaller and ΔCR is decreased. Although ΔCR comes to 0 in the experiment as θ increases, ΔCR in the CFD does not have such a tendency. This discrepancy is caused by the way the vortex is disturbed by the microflap, the detail of which will be shown later.

Distribution of ΔCR on Wing Surface

To see from where the rolling moment is generated, the surface distribution of ΔCR for each flap angle is shown in Fig. 9. The dark part, which has positive values of ΔCR, causes wing-tip-up motion, whereas the white part, which has negative values, causes wing-tip-down motion. At $\theta = 40$ deg, a positive ΔCR region appears near the apex of the delta wing and a negative ΔCR region is predominantly seen at the leading edge. At $\theta = 70$ deg, a positive ΔCR region is produced outboard of the wing at $X/L = 0.5$, and a negative region is inboard, so that integration of ΔCR becomes a positive value (i.e., wing-tip-up motion). When θ increases to 120 deg, a positive ΔCR region is generated inboard of the wing. Furthermore, at $\theta = 160$ deg, the negative values become amplified outboard of the wing as well as the positive values. This ΔCR pattern is opposite that for the case of $\theta = 70$ deg. These distributions are produced as a result of a change in the location and size of LESV, which will be mentioned in the subsequent section.

Flowfield in a Cross Section

Figure 10 shows velocity magnitude contours and particle traces in the cross section of $X/L = 0.5$, where the black part indicates small velocity magnitude, which well represents the difference in

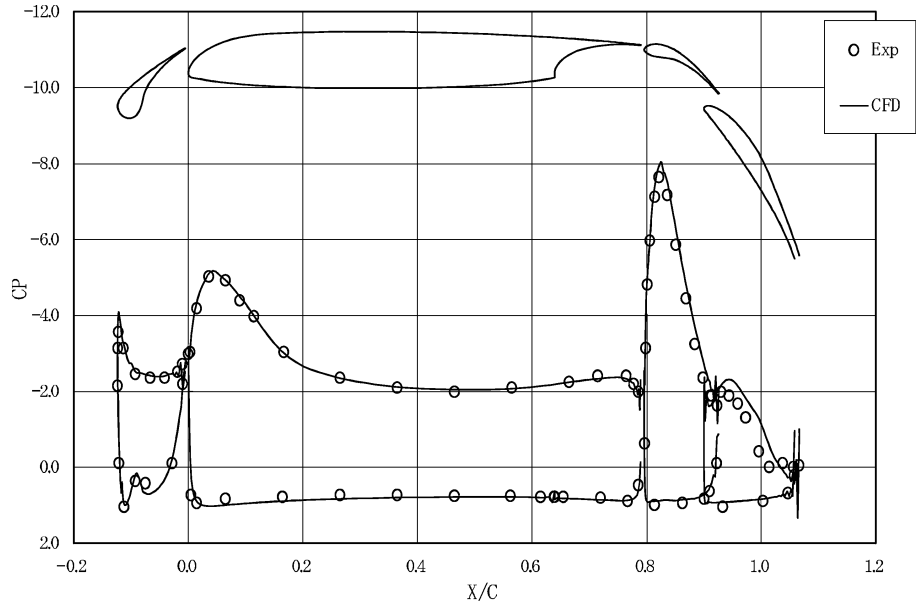

a) $\alpha = 0$ deg

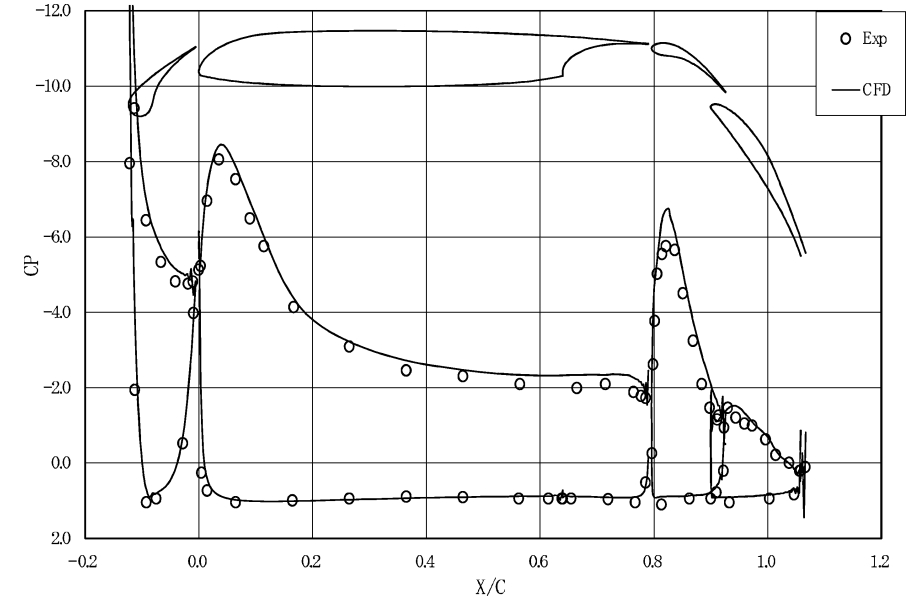

b) $\alpha = 12.2$ deg

Fig. 6 Surface-pressure distribution on multi-element airfoil.

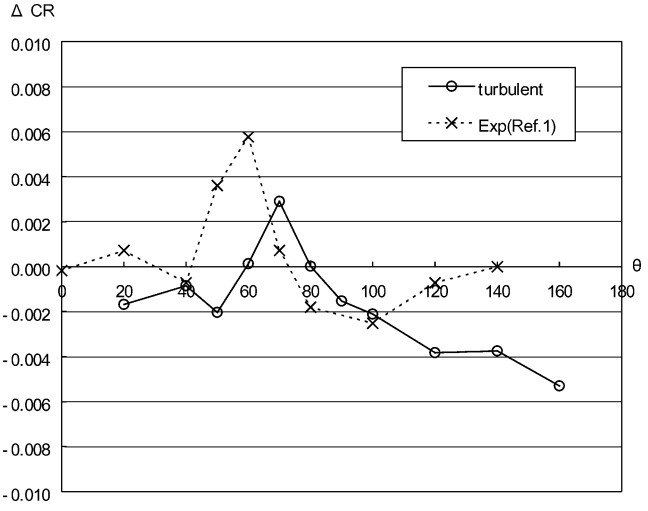

Fig. 7 Change of rolling moment due to tab location in turbulent case.

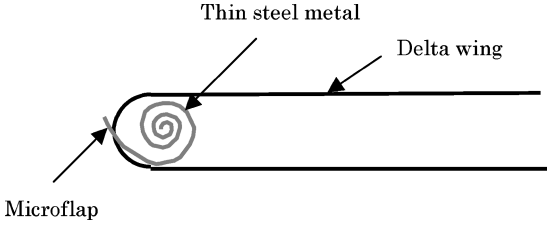

Fig. 8 Detailed mechanics of experimental model.

flow characteristics between flap-off and flap-on cases. Even at $\theta = 40$ deg, the flow over the microflap is influenced. The flow is decelerated just after the flap and reattaches to the wing surface. After some distance the flow separates from the surface, which occurs much earlier than in the flap-off flow. When $\theta = 70$ deg, the microflap causes a complete flow deceleration entirely over the upper wing surface. In addition, the separated flow from the microflap is observed to contain a strong shear layer. When θ increases to 120 deg, flow separation occurs as in the case of

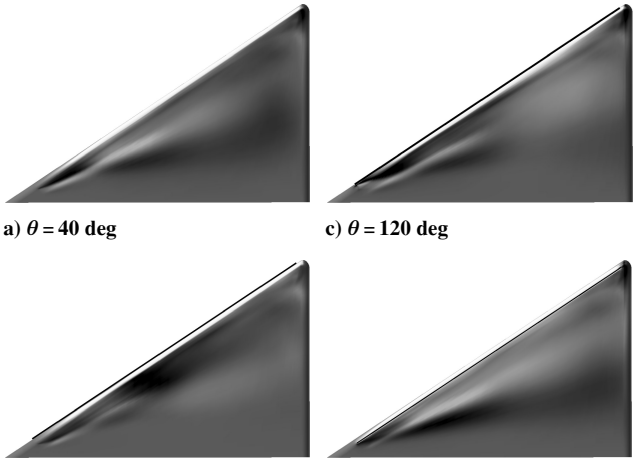

a) $\theta = 40$ deg c) $\theta = 120$ deg

b) $\theta = 70$ deg d) $\theta = 160$ deg

Fig. 9 Surface distributions of ΔCR in turbulent case.

$\theta = 70$ deg, but the degree of flow deceleration is not as large. At $\theta = 160$ deg, the separation point becomes close to that of the flap-off case.

Vorticity contours in the cross section of $X/L = 0.5$ are shown in Fig. 11 for different flap location along with particle traces. The position of the LESV's core in the flap-off case is plotted in each figure with a small open circle. The position of the LESV's core at $\theta = 40$ deg is almost same as that of the flap-off case, but the LESV becomes larger in size and is diffused. At $\theta = 70$ deg, the vortex core moves toward the outboard, which agrees with the description in Ref. 1, and the strength of the shear layer becomes stronger than that of the flap-off case because it generates from the microflap. When θ becomes 120 deg, the shear layer is diffused and the strength of the vortex seems to become weaker, which causes a negative value of ΔCR, as shown in Fig. 7. When θ reaches 160 deg, the vortex core moves toward the inboard and becomes as diffusive as the case where $\theta = 120$ deg. These tendencies can well explain the results of Fig. 7. It should be noted here that the microflap at $\theta \geq 90$ deg diffuses the LESV more because the energy of the flow around the leading edge is reduced.

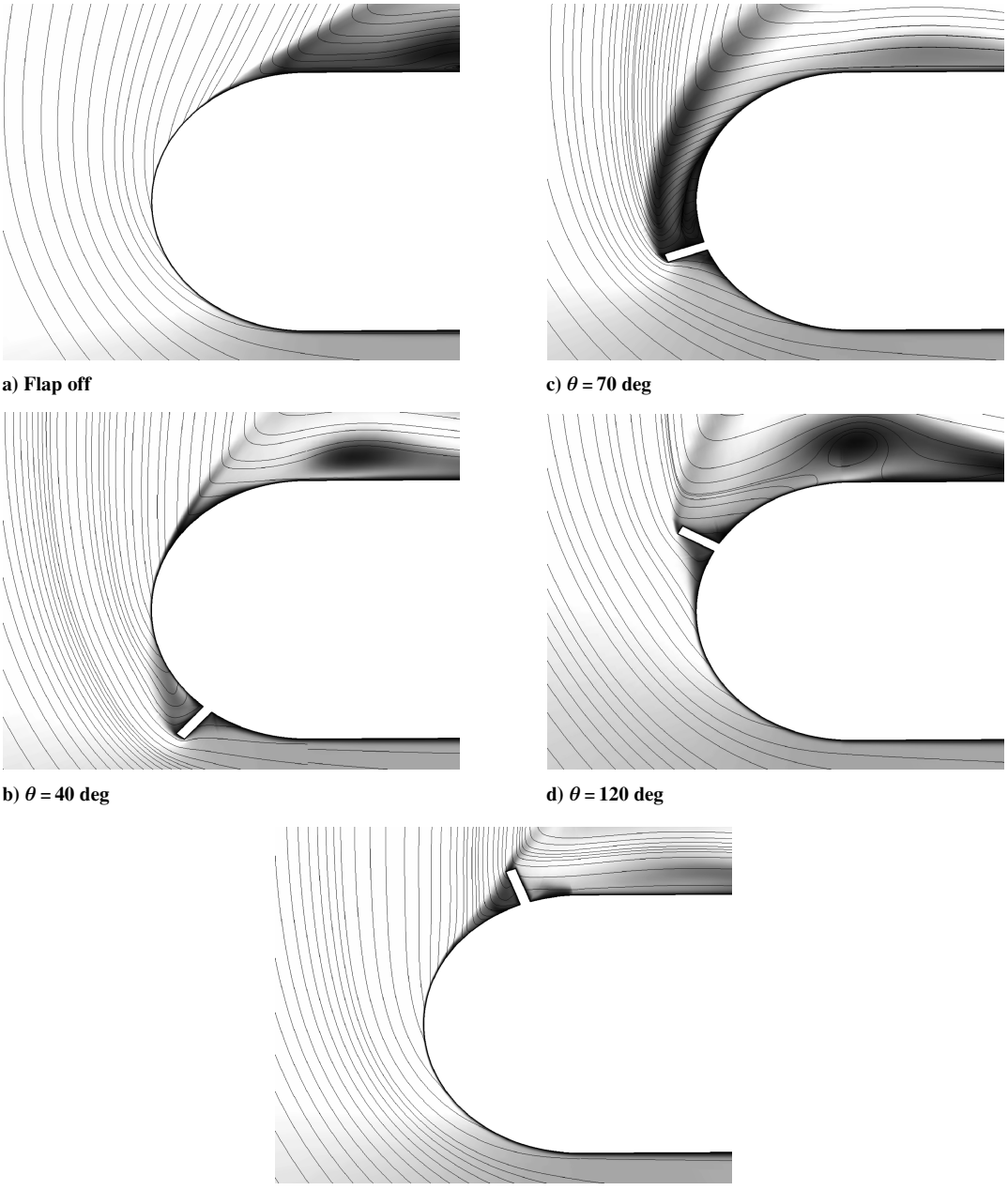

a) Flap off c) $\theta = 70$ deg

b) $\theta = 40$ deg d) $\theta = 120$ deg

e) $\theta = 160$ deg

Fig. 10 Velocity magnitude contours and particle traces at $X/L = 0.5$ in turbulent case.

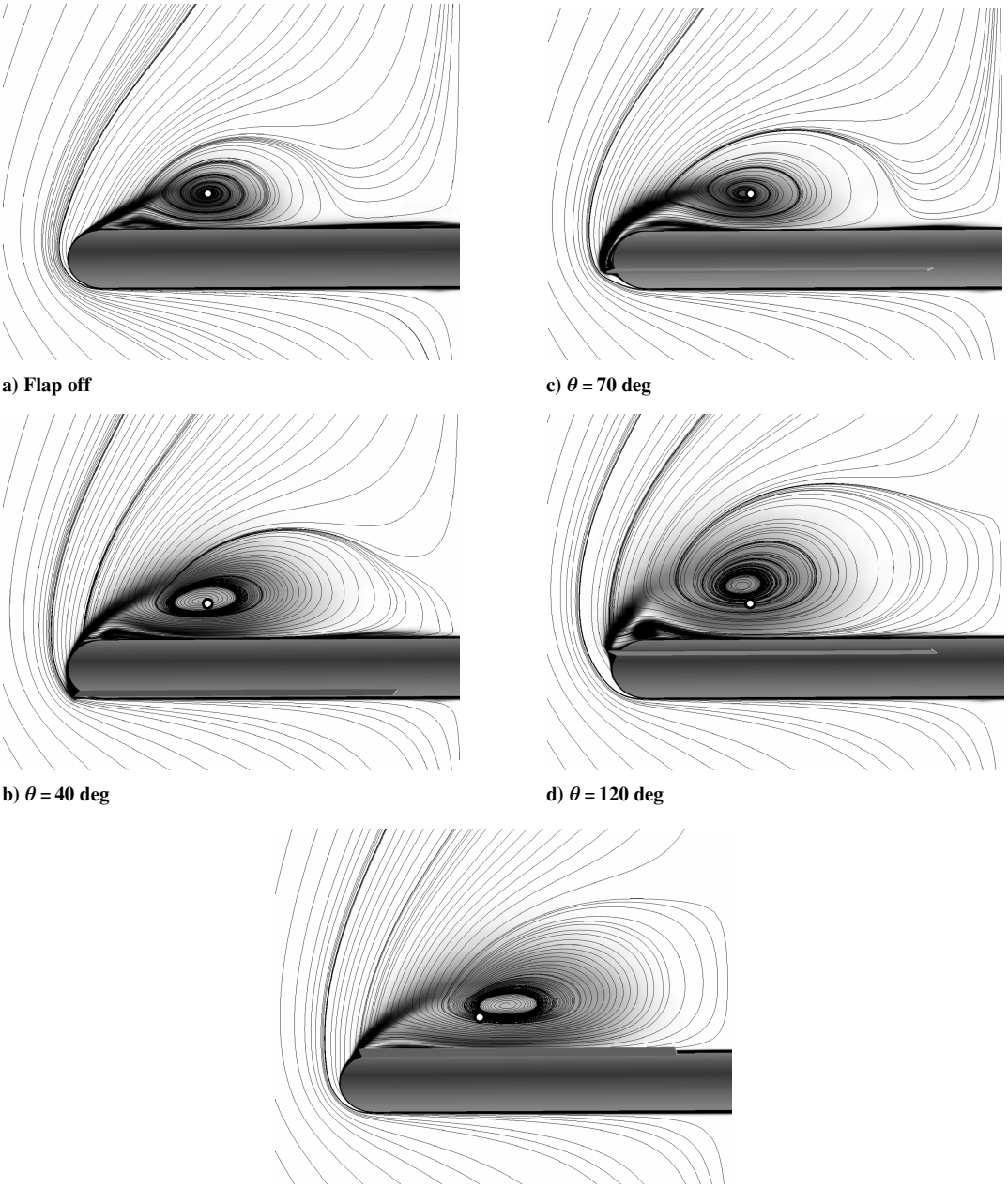

a) Flap off

c) $\theta = 70$ deg

b) $\theta = 40$ deg

d) $\theta = 120$ deg

e) $\theta = 160$ deg

Fig. 11 Vorticity contours and particle traces at $X/L = 0.5$ in turbulent case.

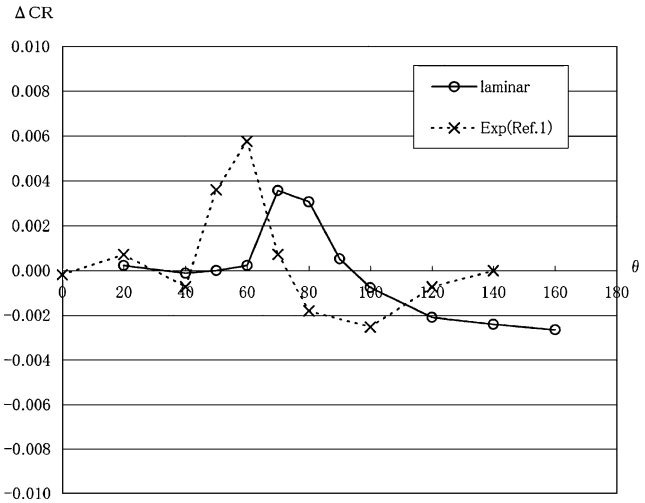

Fig. 12 Change of rolling moment due to tab location in laminar case.

Case 2: Laminar Flow Case

Change in Rolling Moment

The change in rolling moment due to flap location in the laminar flow case is plotted in Fig. 12, which is basically similar to the results of the turbulent case. The ΔCR has positive and negative peaks as in the turbulent case.

Generally, the flap location corresponding to the peak values is close to that in the turbulent case, although they differ from the experimental data. More exactly, the experimental data seem to be shifted by some value toward smaller θ. The reason for this is the same as that for the turbulent case. Moreover, the positive and negative peak values of ΔCR in the laminar case become slightly larger than those of the turbulent case shown in Fig. 7.

Distributions of ΔCR on Wing Surface

The surface distribution of ΔCR for each flap location in the laminar flow case is shown in Fig. 13. The ΔCR distribution at $\theta = 40$ deg is more uniform compared with that in the turbulent case (Fig. 9a). However, at $\theta = 70$ deg, the large positive rolling

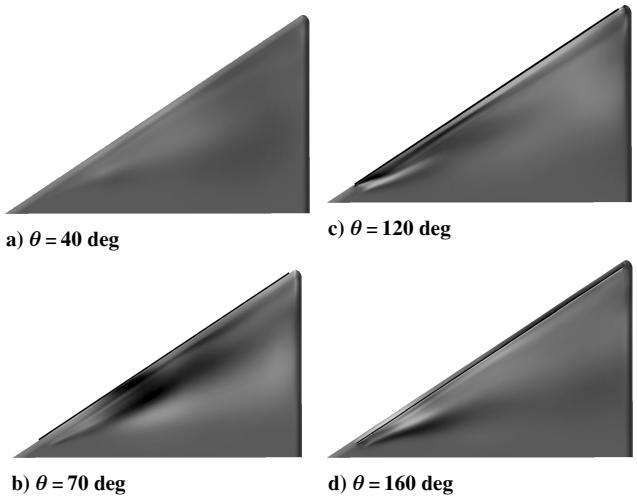

a) $\theta = 40$ deg

c) $\theta = 120$ deg

b) $\theta = 70$ deg

d) $\theta = 160$ deg

Fig. 13 Surface distribution of ΔCR in laminar case.

moment portion depicted in black occurs near the leading edge in the same way as in the corresponding turbulent case. At other larger θ, although the negative region depicted in white is a little smaller than that of the turbulent cases, the pattern also does not differ so greatly between laminar and turbulent cases.

Flowfield in a Cross Section

Figure 14 shows velocity magnitude contours and particle traces in a cross section of $X/L = 0.5$, where flap-off and flap-on cases are compared. At $\theta = 40$ deg, the separation point after the flow reattachment is almost same as that of the flap-off case in spite of the large difference in the turbulent case. At other θ, the flow pattern is basically close to that of the turbulent case shown in Fig. 10.

Vorticity contours and particle traces in the same cross section in the laminar flow case are shown in Fig. 15. As mentioned in the results for the turbulent flow case, the position of the vortex (LESV) core in the flap-off case is plotted in each picture for comparison. At $\theta = 40$ deg, the magnitude of the LESV is almost the same as that for the flap-off case. When θ becomes 70 deg, the vortex core does not move compared with the flap-off case, but the strength

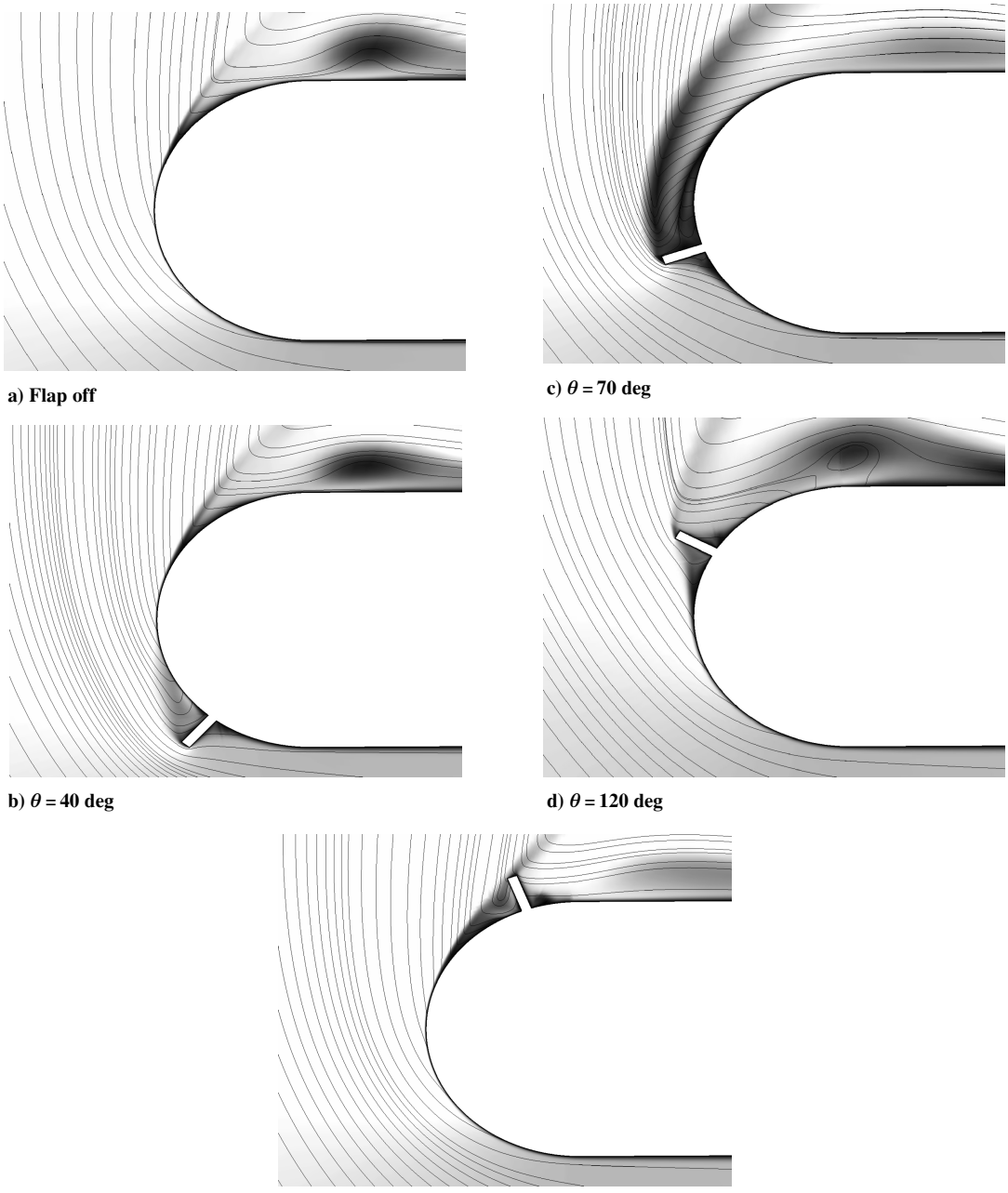

a) Flap off

c) $\theta = 70$ deg

b) $\theta = 40$ deg

d) $\theta = 120$ deg

e) $\theta = 160$ deg

Fig. 14 Velocity magnitude contours and particle traces at $X/L = 0.5$ in laminar case.

Table 1 Comparison between numerical analysis and experiment

θ	Lower installation of flap ($\theta \leqq 90$ deg)	Upper installation of flap ($\theta > 90$ deg)
Present analysis	ΔCR shows a positive peak value at $\theta = 70$ deg. A leading edge separation vortex slightly moves toward outboard in turbulent case and does not almost move in laminar case, but it becomes stronger in both cases.	ΔCR does not show a negative peak between $\theta = 20$ and 160 deg. A leading edge separation vortex moves not in the spanwise direction but further away normally from the upper wing surface. Although the size of the vortex becomes larger, the vortex seems to be diffusive. Beyond $\theta = 120$ deg, the vortex moves toward inboard.
Experiment (Ref. 1)	ΔCR shows a positive peak value at $\theta = 60$ deg. A leading edge separation vortex moves toward outboard.	ΔCR shows a negative peak value at $\theta = 100$ deg. A leading edge separation vortex moves toward inboard.

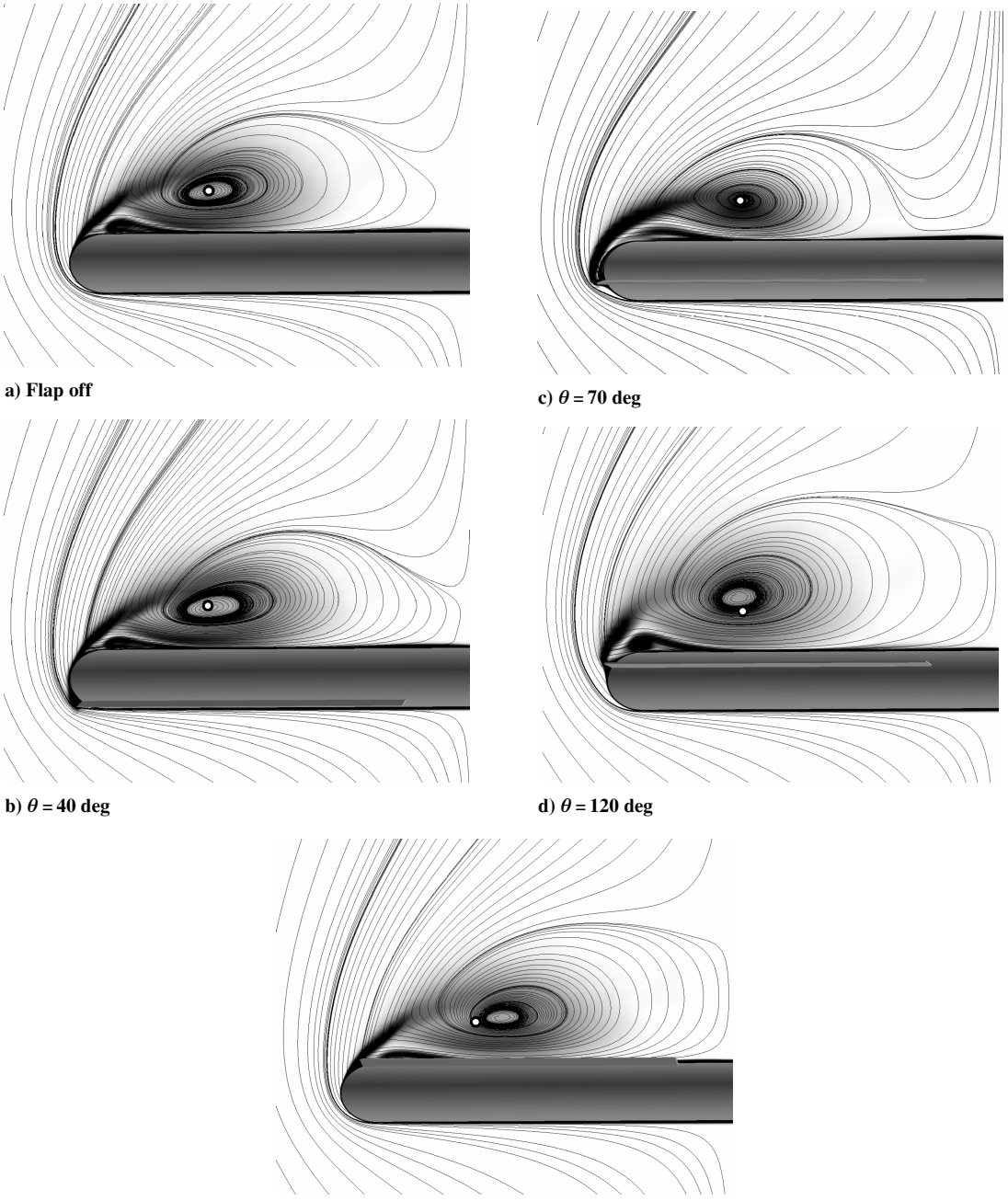

a) Flap off

c) θ = 70 deg

b) θ = 40 deg

d) θ = 120 deg

e) θ = 160 deg

Fig. 15 Vorticity contours and particle traces at X/L = 0.5 in laminar case.

of the shear layer from the microflap becomes stronger so that the rolling moment takes a positive value (see Fig. 12). At $\theta = 120$ deg, although the vortex center comes back to the original position, the vortex moves farther away in the direction normal to the wing surface and its core becomes more diffusive compared with the flap-off case. This is why the rolling moment changes to a negative value at this flap location. When θ increases to 160 deg, the LESV moves toward the inboard and farther away normally from the surface. Consequently, ΔCR becomes negative, as explained in Ref. 1.

Comparison with Experiment

The present results are compared with the experiment of Ref. 1, the summary of which is shown in Table 1. Although detailed data of the experiment are not available, the present simulations for both turbulent and laminar cases capture at least qualitative characteristics of flap effect on rolling moment in a delta wing. The mechanism of rolling moment generation seems to be slightly different from and more complicated than the explanation made based on the experimental data in Ref. 1.

Conclusions

A numerical analysis of aerodynamic force (i.e., rolling moment) generated by a microflap around a delta wing was performed in both turbulent and laminar flow cases. Results of both cases show that the differential rolling moment, that is, the difference in rolling moment between a plain wing and a wing with a flap, is positive at lower flap installation at the leading edge and negative at upper flap installation, which are the same characteristics as those of Ref. 1. However, the mechanism itself is not so simple that we can say definitely that it is due to inboard or outboard movements of LESV. The magnitude and size of the vortex influenced by the microflap also plays an important role in the change in rolling moment. The primary reason why a negative rolling moment is generated by setting the flap at the upper flap location is mainly because of the diffusion of the vortex core in both turbulent and laminar cases. In addition, both turbulent and laminar flows have basically the same effect with regard to the location of the microflap.

Acknowledgments

We are grateful to Ryoyu Keisan Co., Ltd. for the support of this computation. We also would like to thank Ching-Ming Ho and Po-Hao Adam Huang at the University of California, Los Angeles, for their fruitful suggestions and comments on this study.

References

[1]Lee, G. B., Jiang, F., Tsao, T., Tai, Y. C., and Ho, C. M., "Macro Aerodynamic Devices Controlled by Micro Systems," *Proceedings of the IEEE Aerospace and Electronics Systems Society*, Vol. 3, Snowmass, CO, 1997, pp. 255–263.

[2]Guy, Y., Morton, S. A., and Morrow, J. A., "Numerical Investigation of the Flow Field on a Delta Wing with Periodic Blowing and Suction," AIAA Paper 2000-2321, June 2000.

[3]Hassan, A. A., and Munts, E. A., "Transverse and Near-Tangent Synthetic Jets for Aerodynamic Flow Control," AIAA Paper 2000-4334, Aug. 2000.

[4]Roos, F. W., "MICROBLOWING: An Effective, Efficient Method of Vortex-Asymmetry Management(Invited)," AIAA Paper 2000-4416, Aug. 2000.

[5]Kaiden, T., and Nakamura, Y., "Numerical Analysis of Aerodynamic Control by Micro-Flap Around Delta Wing," AIAA Paper 2001-2441, June 2001.

[6]Matsuno, T., Yokouchi, S., Kaiden, T., and Nakamura, Y., "Flow Control on a 45 Degree Delta Wing Using a Small Flap," AIAA Paper 2002-0558, Jan. 2002.

[7]Kaiden, T., and Tamura, Y., "Time Accurate Numerical Simulation of Separation between H-II and SRB," *Proceedings of the 5th International Symposium on Computational Fluid Dynamics*, Sendai, Vol. 1, 1993, pp. 408–413.

[8]Kaiden, T., Shibata, M., and Iwamiya, T., "Numerical Simulation with Bleed and Bypass Effects of Nacelles on SST," *Proceedings of the International CFD Workshop for Super-Sonic Transport Design*, National Aerospace Lab., Tokyo, Japan, 1998, pp. 5–14.

[9]Kamiya, H., Kaiden, T., and Masuda, K., "Numerical Simulation of SST with Nacelle Installation and Flap Deployment," AIAA Paper 2001-1007, Jan. 2001.

[10]Fujii, K., and Obayashi, S., "High-Resolution Upwind Scheme for Vortical-Flow Simulations," *Journal of Aircraft*, Vol. 26, No. 12, 1989, pp. 1123–1129.

[11]Baldwin, B. S., and Lomax, H., "Thin Layer Approximation and Algebraic Model for Separated Turbulent Flows," AIAA Paper 78-257, Jan. 1978.

[12]Degani, D., and Schiff, B. L., "Computation of Turbulent Supersonic Flows Around Pointed Bodies Having Crossflow Separation," *Journal of Computational Physics*, Vol. 66, No. 1, 1986, pp. 173–196.